



Single solid oxide fuel cell modeling and optimization

H. Wen^a, J.C. Ordonez^{a,*}, J.V.C. Vargas^b

^a Department of Mechanical Engineering and Center for Advanced Power Systems, Florida State University, Tallahassee, FL 32310-6046, USA

^b Departamento de Engenharia Mecânica, Universidade Federal do Paraná, C.P. 19011, Curitiba, Paraná 81531-990, Brazil

ARTICLE INFO

Article history:

Received 23 August 2010

Received in revised form 6 October 2010

Accepted 7 October 2010

Available online 24 February 2011

Keywords:

Solid oxide fuel cell
Volume element method
Constructal theory
Optimization
Internal structure

ABSTRACT

In this paper a dynamic model of a single solid oxide fuel cell (SOFC) is developed using a volume element methodology. It consists of a set of algebraic and ordinary differential equations derived from physical laws (e.g., the first law of thermodynamics, Fick's law, and Fourier's law), which allow for the prediction of the temperature and pressure spatial distribution inside the single SOFC, as functions of geometric and operating parameters. The thermodynamic model is coupled with an electrochemical model that is capable of determining the voltage, current, and power output. Based on the simulation results, the internal configuration (structure of the positive electrode–electrolyte–negative electrode assembly) and the operating conditions (air stoichiometric ratio and fuel utilization factor), as well as their impact on the performance of the single SOFC are discussed. Optimal geometric and operating parameters are obtained so that electrical power of the single SOFC at the nominal operating point is maximized. The method used is general and the fundamental optimization results are sharp, showing up to a 357% single SOFC performance variation within the studied parameters' range, therefore these findings show the potential to use the model as a tool for future SOFC design, simulation and optimization.

© 2011 Elsevier B.V. All rights reserved.

1. Introduction

Fuel cells are electrochemical devices that convert chemical energy in fuels directly to electricity. Unlike the conventional power generation methods, there are no intermediate steps such as producing heat by burning fuels and converting it to mechanical work with a heat engine. Thus, the fuel cells are not restricted by some thermodynamic limitations and have high energy efficiency. Besides, except for the small amount of CO₂ emitted as the byproduct of hydrogen generation from hydrocarbon compounds, fuel cells exert minimum impact on the environment. Because of all these virtues, they are considered as one of the most attractive solutions for clean power systems and receive widespread attention from the automotive and power generation industry, as well as many research/academic organizations [1].

Among different types of fuel cells, solid oxide fuel cells (SOFCs) are particularly attractive due to their special features: great fuel flexibility, the feasibility of fuel internal reforming, high energy conversion efficiency, low emission and noise, and the potential application in the highly efficient cogeneration power systems. However, there are key challenges to be overcome before their mass production and widespread application, such as power density aug-

mentation, operating condition control and fuel cell configuration optimization.

Much research and development has been devoted to SOFCs and published in the scientific literature. Virkar et al. [2] discussed the effect of electrode microstructure on activation and concentration potential losses in the SOFC, where the concept of effective charge transfer resistance was introduced. Chan et al. [3] presented a complete polarization model of SOFC that could work under different design and operating conditions. Sorrentino et al. [4] built a 1D model for the planar SOFC and validated it with the experimental data from Pacific Northwest National Laboratory. In the paper, the effects of the several important operating variables on SOFC performance were evaluated, such as the fuel utilization factor, operating temperature and pressure. Vargas et al. [5] built a 1D model for a PEM fuel cell, and with a structured procedure, optimized the internal and external structure of the PEM fuel cell to achieve the maximum net power under different stoichiometric ratios. The model was further validated with the experiment data by Martins et al. [6]. Based on the model of the unit PEM fuel cell, Vargas et al. [7] developed a model for PEM fuel cell stacks and the effect of internal and external configuration on stack performance was discussed. For SOFCs, Ordonez et al. [8] optimized geometric features of a single SOFC based on a simplified model.

Young [9] and Ma et al. [10] recently reviewed the status of three-dimensional SOFC modeling. Young [9] discussed current thermo-fluid modeling capabilities for PEM fuel cell and SOFCs, and highlighted key challenges such as gas diffusion in the porous

* Corresponding author. Tel.: +1 850 644 8405; fax: +1 850 644 7456.
E-mail address: jordonez@fsu.edu (J.C. Ordonez).

Nomenclature

A	area, m^2
A'_{opt}	area of the active TPB regions, m^2
c	molar specific heat, $J mol^{-1} K^{-1}$
c_v	specific heat capacity at constant volume, $J mol^{-1} K^{-1}$
c_p	specific heat capacity at constant pressure, $J kg^{-1} K^{-1}$
D	mass diffusivity, $m^2 s^{-1}$
D_h	gas channel hydraulic diameter, m
D_p	average diameter of the pore, m
D_w	width of a corrugation, m
E	activation energy, $J mol^{-1}$
f	friction factor
F	Faraday's constant, $C equiv^{-1}$
h	heat transfer coefficient, $W m^{-2} K^{-1}$
H	enthalpy, $J mol^{-1}$
i	current density, $A m^{-2}$
i_0	exchange current density, $A m^{-2}$
i_{as}	limiting current density (anode-limited), $A m^{-2}$
i_{cs}	limiting current density (cathode-limited), $A m^{-2}$
I	working current, A
k	thermal conductivity, $W m^{-1} K^{-1}$
L	length, m
L'	reaction region thickness, m
L'_{opt}	active TPB region thickness, m
m	mass, kg
\dot{m}	mass flow rate, $kg s^{-1}$
M	molecular weight, $kg mol^{-1}$
n	equivalent electron per mole of reactant, equiv. mol^{-1}
\dot{n}	molar rate involved in the electrochemical reaction, $mol s^{-1}$
\dot{n}_{in}	molar flow rate at the inlet, $mol s^{-1}$
\dot{n}_{out}	molar flow rate at the outlet, $mol s^{-1}$
n_{ch}	number of channels
$n_{m,i}$	number of moles of component i in the mixture
$n_{m,T}$	total number of moles in the mixture
N	heat capacity, $J K^{-1}$
p	pressure, Pa
P	dimensionless pressure
Pr	Prandtl number
Q	heat transfer rate, W
R	universal gas constant, $J mol^{-1} K^{-1}$
R_j	specific gas constant, $J kg^{-1} K^{-1}$
Re	Reynolds number
S^0	standard entropy, $J mol^{-1} K^{-1}$
t	time, s
T	temperature, K
u	velocity, $m s^{-1}$
V	voltage, V
V_T	total volume of the single SOFC, m^3
W	power, W
W_E	electric power, W
W_N	net power, W
W_P	pumping power, W
X	molar fraction of component in the mixture
Zr	grain size, m

Greek symbols

α	fraction of the reaction heat that is generated at the anode
α_c	charge transfer coefficient

α_t	anode thermal diffusivity
β	ohmic resistance, Ω
χ	gas channel aspect ratio
δ	pre-exponential factor, $\Omega^{-1} m^{-2}$
ε	emissivity
ϕ	porosity
γ_f	fuel utilization factor
η	overpotential, V
θ	dimensionless temperature
ξ	dimensionless length
τ	dimensionless time
λ_{air}	stoichiometric ratio
μ	viscosity, $Pa s$
ν	diffusion volume of simple molecules, cm^3
ρ	density, $kg m^{-3}$
σ	electrical conductivity, $\Omega^{-1} m^{-1}$
σ_{rad}	Stefan–Boltzmann constant
ψ	tortuosity
κ	isentropic index

Subscript and superscript

0	initial condition
1	bipolar plate (interconnect)
2	fuel channel or fuel
3	anode
4	electrolyte
5	cathode
6	air channel or air
~	dimensionless
a	anode
act	activation
actconc	activation and concentration
active	the active reaction region
air	air
c	cathode
ch	channel
cnd	conduction
cnv	convection
conc	concentration
eff	effective
f	fuel
h	hydraulic
in	inlet
H ₂	hydrogen
H ₂ O	water
in	inlet
limit	limit
mm	two-way maximum
mmm	three-way maximum
mass	mass transfer
N ₂	nitrogen
n	nominal operating point
o	standard condition [gases at 1 atm, 298.15 K]
O ₂	oxygen
ocp	open circuit potential
ohm	ohmic
opt	optimal
out	outlet
rad	radiation
ref	reference
rct	reaction
t	channel shoulder
total	total

TPB	three-phase boundary
x	x direction
y	y direction
z	z direction

layer, the internal fuel reforming rate and the transport of gas species, ions, and electrons accompanied with the electrochemical reaction. Ma et al. [10] reviewed the current computational fluid dynamics (CFD) modeling of fuel cells. Bove and Ubertini [11] developed a complete three-dimensional, time-dependent SOFC numerical model which accounts for various phenomena occurring in each component of the fuel cell. Janardhanan and Deutschmann [12] made CFD analysis of an internally reforming anode supported SOFC button cell, which accounts for the heterogeneous fuel reforming chemistry, electrochemistry and porous media transport inside the fuel cell. In the paper the effect of steam content in the anode feed stream on the resulting overpotential losses and surface coverages of various species at the three-phase boundary were discussed. Furthermore, Janardhanan et al. [13] introduced a mathematical model to calculate the volume specific three-phase boundary length in the porous composite electrodes of SOFC, which is of crucial importance to the SOFC performance.

Though very useful refined spatial information can be extracted from three-dimensional models, the computational time requirements prevent their use for optimization strategies in which multiple runs for different geometries and operating conditions are necessary. As a result, there is a need for an efficient computational methodology, which captures the dominant physical and electrochemical phenomena occurring in SOFC and is accurate enough to depict the response of the single SOFC under different internal configurations and operating conditions.

In this paper a one-dimensional single SOFC model based on the fundamental physical laws is presented. The single SOFC is divided into six lumped control volumes that correspond to the most representative parts of a single fuel cell. The phenomena such as heat and mass transfer, fluid flow, electrochemical reaction, potential losses and power consumption and generation are taken into account, and the solution includes the temperature and pressure field in each control volume, the polarization curves and the power output of the single SOFC. Based on the simulation results obtained with the model, the effects of operating parameters, such as air stoichiometric ratio and fuel utilization factor, as well as the PEN (positive electrode–electrolyte–negative electrode assembly) internal structure on SOFC performance are investigated. Finally, the optimal values for each investigated design and operating parameter of the single SOFC are proposed for maximum fuel cell performance.

2. Thermal model

The configuration of a single SOFC is shown in Fig. 1. It consists of six control volumes: the solid bipolar plate–interconnect (CV1), the fuel channels (CV2), the anode layer (CV3), the electrolyte layer (CV4), the cathode layer (CV5), and the oxidant channels (CV6).

The fuel and oxidant supplied at the channels diffuse through the anode layer and cathode layer, respectively, where they react separately at the ionic conductor/electronic conductor/gas interface (three phase boundaries, TPB). The bipolar plate (interconnect) provides a series of electrical connectors to the adjacent cells or to the external circuit, and at the same time serves as a gas barrier between the fuel channels and oxidant channels of adjacent cells.

A wide range of fuels could be used in the electrochemical reaction of SOFC, including various hydrocarbon fuels. For simplicity, in

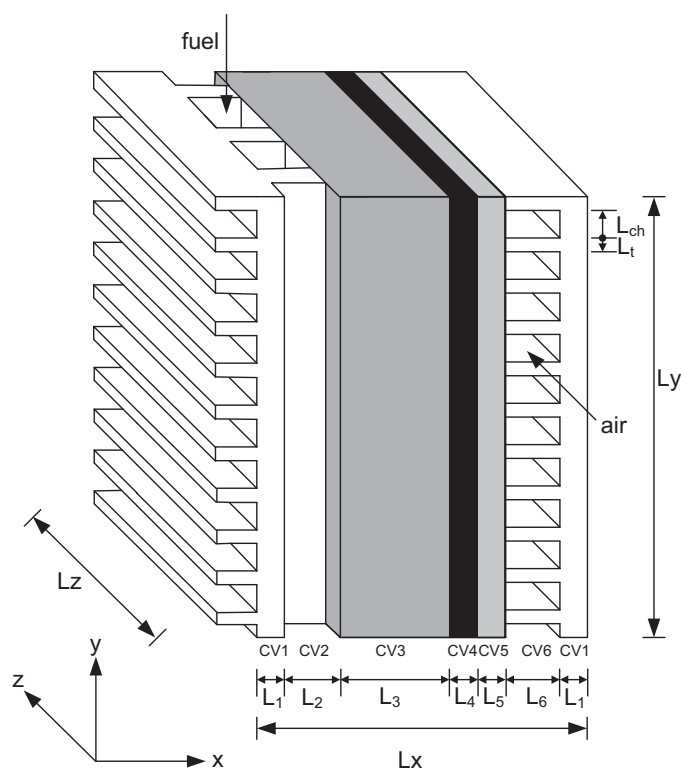


Fig. 1. The 3D configuration of a planar single SOFC.

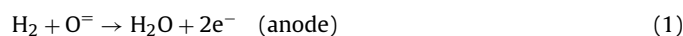
this paper pure hydrogen and air are considered as fuel and oxidant, respectively.

Due to the heat and mass interaction inside the single SOFC, the thermal model includes mass and energy conservation equations for each control volume, as well as the electrochemical reaction equations at the two electrodes. The electrochemical model uses the temperature and pressure fields in the evaluation of the performance of the single SOFC.

The electrochemical model contains the analysis and computation of reversible electrical potential and various kinds of losses, such as the losses due to surface overpotentials (poor electrocatalysis), slow diffusion and all internal ohmic losses through the cell. The actual cell potential results from the reversible electrical potential by subtracting all the losses, which are functions of the working current, temperature and pressure, and SOFC configuration. The computation of the actual electrical power output from the SOFC and the power consumed pumping fuel and oxidant into the gas channels are also included in the model to obtain the net power output.

2.1. Mass balances in the fuel and air channels

In a single SOFC, there are electrochemical reactions both in the anode layer and the cathode layer. These reactions are expressed by the equations:



The hydrogen in the anode layer and the oxygen in the cathode layer are supplied by the fuel channels and oxidant channels, respectively. Based on the electrochemical reaction equations, the molar flow rate of hydrogen at the inlet and outlet of fuel channels, as well as hydrogen consumed by the electrochemical reaction, are

determined by the working current (I):

$$\begin{aligned}\dot{n}_{\text{H}_2,\text{in}} &= \frac{I}{nF\gamma_f} = \frac{I}{2F\gamma_f}, & \dot{n}_{\text{H}_2,\text{out}} &= \frac{I}{nF} \left(\frac{1}{\gamma_f} - 1 \right) = \frac{I}{2F} \left(\frac{1}{\gamma_f} - 1 \right), \\ \dot{n}_{\text{H}_2} &= \frac{I}{nF} = \frac{I}{2F}\end{aligned}\quad (3)$$

where n is the number of mols of electrons transferred per mol of reactant, for the hydrogen $n=2$, and for the oxygen $n=4$. F is the Faraday constant, 96500 C mol^{-1} , and γ_f ($\gamma_f \leq 1$) is the fuel utilization factor and defined as the ratio between the fuel consumed in the reaction and the fuel supplied in the fuel channels.

In the fuel channels, the average molar fractions $X_i = n_{m,i}/n_{m,T}$, defined as the average number of mols of component i divided by the total number of mols of the mixture, is approximated as:

$$X_{\text{H}_2\text{O}} = \frac{\gamma_f}{2}, \quad X_{\text{H}_2} = 1 - \frac{\gamma_f}{2} \quad (4)$$

Similarly, the molar flow rate of oxygen at the inlet and outlet of air channels and the oxygen consumed by the electrochemical reaction are:

$$\begin{aligned}\dot{n}_{\text{O}_2,\text{in}} &= \frac{I}{nF}\lambda_{\text{air}} = \frac{I}{4F}\lambda_{\text{air}}, & \dot{n}_{\text{O}_2,\text{out}} &= (\lambda_{\text{air}} - 1)\frac{I}{nF} = (\lambda_{\text{air}} - 1)\frac{I}{4F}, \\ \dot{n}_{\text{O}_2} &= \frac{I}{nF} = \frac{I}{4F}\end{aligned}\quad (5)$$

where λ_{air} is the air stoichiometric ratio, and defined as the air provided in the channels divided by the air needed for the electrochemical reaction of interest.

In the present study, the oxidant provided in the oxidant channels is air, which is assumed to be composed of oxygen and nitrogen only. The molar flow rate of nitrogen at the inlet and outlet are obtained as:

$$\dot{n}_{\text{N}_2,\text{in}} = \dot{n}_{\text{N}_2,\text{out}} = \frac{I\lambda_{\text{air}}X_{\text{N}_2,\text{in}}}{nFX_{\text{O}_2,\text{in}}} = \frac{I\lambda_{\text{air}}X_{\text{N}_2,\text{in}}}{4FX_{\text{O}_2,\text{in}}} \quad (6)$$

The average molar fractions of oxygen and nitrogen in the oxidant channels are

$$\begin{aligned}X_{\text{O}_2} &= \frac{2\lambda_{\text{air}}X_{\text{O}_2,\text{in}} - X_{\text{O}_2,\text{in}} - X_{\text{O}_2,\text{in}}^2}{2(\lambda_{\text{air}} - X_{\text{O}_2,\text{in}})}, \\ X_{\text{N}_2} &= \frac{2\lambda_{\text{air}}X_{\text{N}_2,\text{in}} - X_{\text{O}_2,\text{in}}X_{\text{N}_2,\text{in}}}{2(\lambda_{\text{air}} - X_{\text{O}_2,\text{in}})}\end{aligned}\quad (7)$$

2.2. Energy balances

2.2.1. Dimensionless variables

The application of the first law of thermodynamics to every control volume of the single SOFC illustrated in Fig. 1 yields expressions for their temperature variations during the heat and mass transfer processes associated with the SOFC operation. In addition, to simplify the acquired equations, they are written in dimensionless form and all the quantities in them are rescaled to values as close as possible to 1, which in turn simplifies the numerical calculations.

In a dimensionless model, all variables are directly proportional to the actual dimensional ones. Therefore, this allows for scaling up or down any system with similar characteristics to the system analyzed by the model. Another important aspect is that any dimensionless variable value used in the simulations could represent an entire and numerous set of dimensional values by varying appropriately the parameters in the dimensionless variables definition, which by itself stresses the generality of the dimensionless model. Physically, the set of results of a dimensionless model actually represents the expected system response to numerous combinations of system parameters (geometry, architecture) and operating

conditions (e.g., ambient conditions and mass flow rates), without having to simulate each of them individually, as a dimensional model would require. Based on that reasoning, it is convenient to search for an alternative formulation that eliminates the physical dimensions of the problem.

For instance, all the actual lengths in the model are nondimensionalized in the following way, from which their corresponding dimensionless lengths are obtained:

$$\xi_i = \frac{L_i}{V_T^{1/3}}, \quad i = 1, 2, 3, 4, 5, 6, \text{ t, ch, x, y, z}$$

where $V_T = L_x L_y L_z$ represents the total volume of the single SOFC.

Similarly, the dimensionless temperatures are defined as:

$$\theta_i = \frac{T_i}{T_{\text{ref}}}, \quad i = 1, 2, 3, 4, 5, 6$$

where T_{ref} is referenced to the ambient temperature. The dimensionless pressures are:

$$P_i = \frac{p_i}{p_{\text{ref}}}, \quad i = \text{H}_2, \text{O}_2, \text{H}_2\text{O}, \text{N}_2, \text{air, f, TPB}$$

where p_{ref} is referenced to the ambient pressure.

Other dimensionless quantities include:

The dimensionless time $\tau = t/t_{\text{ref}}$, where $t_{\text{ref}} = (4V_T^{2/3})/\alpha_t$ and $\alpha_t = k_3/(\rho_3 c_{p,3})$ refers to the thermal diffusivity of the anode.

The dimensionless area $\tilde{A}_i = A_i/(V_T^{2/3})$.

The dimensionless mass $\tilde{m}_i = m_i/m_{\text{ref}}$, where $m_{\text{ref}} = \rho_3 V_T$.

The dimensionless mass flow rate $\tilde{\dot{m}}_i = \dot{m}_i/\dot{m}_{\text{ref}}$, where $\dot{m}_{\text{ref}} = (\rho_3 V_T)/t_{\text{ref}}$.

The dimensionless thermal conductivity $\tilde{k}_i = (k_i V_T^{1/3})/(\dot{m}_{\text{ref}} c_{p,f})$.

The dimensionless convective heat transfer coefficient $\tilde{h}_i = (h_i V_T^{2/3})/(\dot{m}_{\text{ref}} c_{p,f})$.

The dimensionless Stefan-Boltzmann constant $\tilde{\sigma}_{\text{rad}} = (\sigma_{\text{rad}} V_T^{2/3} T_{\text{ref}}^3)/(\dot{m}_{\text{ref}} c_{p,f})$.

The dimensionless heat transfer rate and power $\tilde{Q}_i = Q_i/(\dot{m}_{\text{ref}} c_{p,f} T_{\text{ref}})$ and $\tilde{W}_i = W_i/(\dot{m}_{\text{ref}} c_{p,f} T_{\text{ref}})$.

In all the equations above, the subscript i indicates a substance or a location in the fuel cell.

2.2.2. Energy conservation

The thermal model consists of six ordinary differential equations which are derived by applying the energy conservation law to each control volume. In the present study the single SOFC is considered to be an internal cell in a SOFC stack and has the interaction with its adjacent cells. It is also assumed that the adjacent cells have similar internal temperature profiles.

For CV1, energy conservation states that:

$$\frac{d\theta_1}{d\tau} = \frac{(\tilde{Q}_{\text{rad},1-3} + \tilde{Q}_{\text{rad},1-5} + \tilde{Q}_{\text{cnv},1-2} + \tilde{Q}_{\text{cnv},1-6} + \tilde{Q}_{\text{ohm},1} + \tilde{Q}_{\text{cnd},1-3} + \tilde{Q}_{\text{cnd},1-5})}{\tilde{N}_1} \quad (8)$$

where the dimensionless heat capacities, \tilde{N}_i , are given as:

$$\tilde{N}_i = \frac{m_i c_{p,i}}{m_{\text{ref}} c_{p,f}}, \quad i = 1, 3, 4, 5 \quad (9)$$

where $m_1 = \rho_1 [L_1 L_y L_z + (L_y L_2 + L_6 L_z)L_t (n_{\text{ch}} + 1)]$ and $m_i = \rho_i L_y L_z L_i$, $i = 3, 4, 5$.

In Eq. (8), the radiation heat transfer from the anode layer and cathode layer to the bipolar plate are:

$$\tilde{Q}_{\text{rad},1-j} = \tilde{A}_{\text{rad},j} \tilde{\sigma}_{\text{rad}} \varepsilon_{\text{eff},j} (\theta_j^4 - \theta_1^4), \quad j = 3, 5 \quad (10)$$

where $\tilde{A}_{\text{rad},3} = (n_{\text{ch}} L_{\text{ch}} L_y)/(V_T^{2/3})$ and $\tilde{A}_{\text{rad},5} = (n_{\text{ch}} L_{\text{ch}} L_z)/(V_T^{2/3})$ are the dimensionless radiation heat transfer areas between the electrodes and the bipolar plate.

The effective emissivities are estimated by [14]:

$$\epsilon_{\text{eff},3} = \frac{1}{1/\epsilon_3 + (L_{\text{ch}}/(L_{\text{ch}} + 2L_2))(1/\epsilon_1 - 1)} \quad (11a)$$

$$\epsilon_{\text{eff},5} = \frac{1}{1/\epsilon_5 + (L_{\text{ch}}/(L_{\text{ch}} + 2L_6))(1/\epsilon_1 - 1)} \quad (11b)$$

In Eq. (8), the heat conduction from the anode layer and the cathode layer to the bipolar plate are:

$$\tilde{Q}_{\text{cnd},1-3} = \frac{2\tilde{A}_{\text{cnd},3}(\theta_3 - \theta_1)\tilde{k}_3\tilde{k}_1}{(\xi_3\tilde{k}_1 + \xi_2\tilde{k}_3)} \quad (12a)$$

$$\tilde{Q}_{\text{cnd},1-5} = \frac{2\tilde{A}_{\text{cnd},5}(\theta_5 - \theta_1)\tilde{k}_5\tilde{k}_1}{(\xi_5\tilde{k}_1 + \xi_6\tilde{k}_5)} \quad (12b)$$

where $\tilde{A}_{\text{cnd},3} = (1 - \phi_3)(n_{\text{ch}} + 1)\xi_t\xi_y$ and $\tilde{A}_{\text{cnd},5} = (1 - \phi_5)(n_{\text{ch}} + 1)\xi_t\xi_z$ stand for the conduction heat transfer areas between bipolar plate and electrodes. ϕ_3 and ϕ_5 represent the anode and cathode porosities, respectively.

In addition, the dimensionless convective heat transfer from fuel channels and oxidant channels to the bipolar plate are expressed as:

$$\tilde{Q}_{\text{cnv},1-j} = \tilde{h}_j\tilde{A}_{\text{cnv},j}(\theta_j - \theta_1), \quad j = 2, 6 \quad (13)$$

where $\tilde{A}_{\text{cnv},2} = n_{\text{ch}}(\xi_{\text{ch}} + 2\xi_2)\xi_y$ and $\tilde{A}_{\text{cnv},6} = n_{\text{ch}}(\xi_{\text{ch}} + 2\xi_6)\xi_z$.

The convective heat transfer coefficients h_j in the fuel and oxidant channels are estimated according to the flow regime. For the laminar flow ($Re_h < 2300$) [15]:

$$f_j Re_{h,j} = 24(1 - 1.3553\chi_j + 1.9467\chi_j^2 - 1.7012\chi_j^3 + 0.9564\chi_j^4 - 0.2537\chi_j^5), \quad j = 2, 6 \quad (14a)$$

$$\frac{h_j D_{h,j}}{k_j} = 7.541(1 - 2.610\chi_j + 4.970\chi_j^2 - 5.119\chi_j^3 + 2.702\chi_j^4 - 0.548\chi_j^5), \quad j = 2, 6 \quad (14b)$$

For the turbulent flow ($2300 < Re_h < 2 \times 10^4$) [16]:

$$f_j = 0.079 Re_{h,j}^{1/4}, \quad j = 2, 6 \quad (14c)$$

$$\frac{h_j D_{h,j}}{k_j} = \frac{(f_j/2)(Re_{h,j} - 1000)Pr_j}{1 + 12.7(f_j/2)^{1/2}(Pr_j^{2/3} - 1)}, \quad j = 2, 6 \quad (14d)$$

where $\chi_j = L_{\text{ch}}/L_j$, when $L_{\text{ch}} \leq L_j$ and $\chi_j = L_j/L_{\text{ch}}$, when $L_{\text{ch}} > L_j$; $D_{h,j} = 2L_{\text{ch}}L_j/(L_{\text{ch}} + L_j)$; Pr is the gas Prandtl number; f is the friction factor.

The Reynolds number is a function of the average flow velocities in the channels u_j , which are approximated in terms of the molar flow rates:

$$u_2 = \frac{R[\dot{n}_{\text{H}_2,\text{in}}T_{\text{f,in}} + (\dot{n}_{\text{H}_2,\text{out}} + \dot{n}_{\text{H}_2\text{O,out}})T_2]}{2p_{\text{f}}L_{\text{ch}}L_2n_{\text{ch}}} \quad (15a)$$

$$u_6 = \frac{R[(\dot{n}_{\text{O}_2,\text{in}} + \dot{n}_{\text{N}_2,\text{in}})T_{\text{air,in}} + (\dot{n}_{\text{O}_2,\text{out}} + \dot{n}_{\text{N}_2,\text{out}})T_6]}{2p_{\text{air}}L_{\text{ch}}L_6n_{\text{ch}}} \quad (15b)$$

The dimensionless ohmic, activation and concentration heating rates are given as follows:

$$\tilde{Q}_{\text{ohm},j} = \frac{\eta_{\text{ohm},j}}{\dot{m}_{\text{ref}}c_{p,\text{f}}T_{\text{ref}}}I, \quad j = 1, 3, 4, 5 \quad (16a)$$

$$\tilde{Q}_{\text{actconc},j} = \frac{\eta_{\text{act},j} + \eta_{\text{conc},j}}{\dot{m}_{\text{ref}}c_{p,\text{f}}T_{\text{ref}}}I, \quad j = 3, 5 \quad (16b)$$

where the activation, concentration and ohmic potential losses in each compartment, $(\eta_{\text{act},j}, \eta_{\text{conc},j}, \eta_{\text{ohm},j})$, are discussed later in the electrochemical model.

In the present study, the fuel channels are open control volumes filled with hydrogen and its oxidation product, i.e., water. It is also assumed that the total pressure in the fuel channels and oxidant channels are known and constant. Applying the energy conservation law to CV2 yields:

$$\frac{d\theta_2}{d\tau} = \frac{[-\tilde{Q}_{\text{cnv},1-2} + \tilde{Q}_{\text{cnv},2-3} + \tilde{Q}_{\text{mass},2}]}{\tilde{N}_2} \quad (17)$$

where the dimensionless heat capacity of CV2, \tilde{N}_2 , is given as follows:

$$\tilde{N}_2 = \frac{p_{\text{f}}n_{\text{ch}}L_{\text{ch}}L_2L_y(X_{\text{H}_2\text{Cv,H}_2} + X_{\text{H}_2\text{O}^{\text{Cv,H}_2\text{O}})}{RT_2m_{\text{ref}}c_{p,\text{f}}} \quad (18)$$

$\tilde{Q}_{\text{cnv},2-3}$ is the dimensionless convective heat transfer between the anode and the fuel channels and calculated by: $\tilde{Q}_{\text{cnv},2-3} = \tilde{h}_2n_{\text{ch}}\xi_{\text{ch}}\xi_y(1 - \phi_3)(\theta_3 - \theta_2)$, where the convective heat transfer coefficient, \tilde{h}_2 , is computed with Eq. (14). $\tilde{Q}_{\text{mass},2}$ stands for the energy variation associated with the mass transfer (fuel and water vapor) in CV2 when they cross the boundaries:

$$\tilde{Q}_{\text{mass},2} = \frac{\dot{n}_{\text{H}_2,\text{in}}(H_{\text{H}_2,\text{f}} - H_{\text{H}_2,2}) + \dot{n}_{\text{H}_2\text{O}}(H_{\text{H}_2\text{O},3} - H_{\text{H}_2\text{O},2})}{\dot{m}_{\text{ref}}c_{p,\text{f}}T_{\text{ref}}} \quad (19)$$

where $\dot{n}_{\text{H}_2\text{O}} = \dot{n}_{\text{H}_2}$.

Heat is generated when the electrochemical reactions expressed by Eqs. (1) and (2) take place. In the present study, it is assumed that the total thermal effect of the two semi-reactions on the temperature profile of the single SOFC can be approximated as one overall electrochemical reaction: $\text{H}_2 + (1/2)\text{O}_2 \rightarrow \text{H}_2\text{O}$, which takes place at the electrolyte temperature T_4 . The total heat generation is given by [17]:

$$\tilde{Q}_{\text{rct}} = \frac{\dot{n}_{\text{H}_2}[-T_4(S_{\text{H}_2\text{O},4}^0 - S_{\text{H}_2,4}^0 - (1/2)S_{\text{O}_2,4}^0) + RT_4 \ln(P_{\text{H}_2\text{O,TPB}}/P_{\text{H}_2,\text{TPB}}(P_{\text{O}_2,\text{TPB}})^{1/2})]}{\dot{m}_{\text{ref}}c_{p,\text{f}}T_{\text{ref}}} \quad (20)$$

Part of the dimensionless reaction heat rate, $\alpha\tilde{Q}_{\text{rct}}$, is generated at the anode ($0 < \alpha < 1$), and the rest, $(1 - \alpha)\tilde{Q}_{\text{rct}}$, is generated at the cathode.

According to the assumption, the standard entropy of formation S^0 in Eq. (20), is evaluated at the electrolyte temperature T_4 . The three-phase boundaries pressures, P_{TPB} , refer to the partial pressures of reactants and products at the place where the electrochemical reaction actually takes place. Equations for the three-phase boundaries pressures are given by Kim et al. [18] and Aguiar et al. [19] with the assumption that three-phase boundaries pressures are uniform within the reaction regions and approximated as the partial pressure at the electrode/electrolyte interface:

$$p_{\text{H}_2\text{O,TPB}} = p_{\text{f}}X_{\text{H}_2\text{O}} + \frac{RT_3\psi_3}{2FD_3\phi_3} \frac{L_3I}{L_yL_z} \quad (21a)$$

$$p_{\text{H}_2,\text{TPB}} = p_{\text{f}}X_{\text{H}_2} - \frac{RT_3\psi_3}{2FD_3\phi_3} \frac{L_3I}{L_yL_z} \quad (21b)$$

$$p_{\text{O}_2,\text{TPB}} = p_{\text{air}} - (p_{\text{air}} - X_{\text{O}_2}p_{\text{air}})\exp\left(\frac{RT_5\psi_5L_5I}{4FD_5\phi_5p_{\text{air}}L_yL_z}\right) \quad (21c)$$

where ψ is the tortuosity, D is the diffusivity, p_{f} is the total pressure in the fuel channels, p_{air} is the total pressure in the oxidant channels. According to Kim et al. [18], binary diffusion dominates the gas transport through the porous electrodes. The diffusivities, D_j , in the anode layer and the cathode layer are obtained from [20]:

$$D_3 = \frac{1.43 \times 10^{-7} T_3^{1.75} (M_{\text{H}_2} + M_{\text{H}_2\text{O}})^{1/2}}{P_{\text{f}}(2M_{\text{H}_2}M_{\text{H}_2\text{O}})^{1/2}(\nu_{\text{H}_2}^{1/3} + \nu_{\text{H}_2\text{O}}^{1/3})^2} \quad (22a)$$

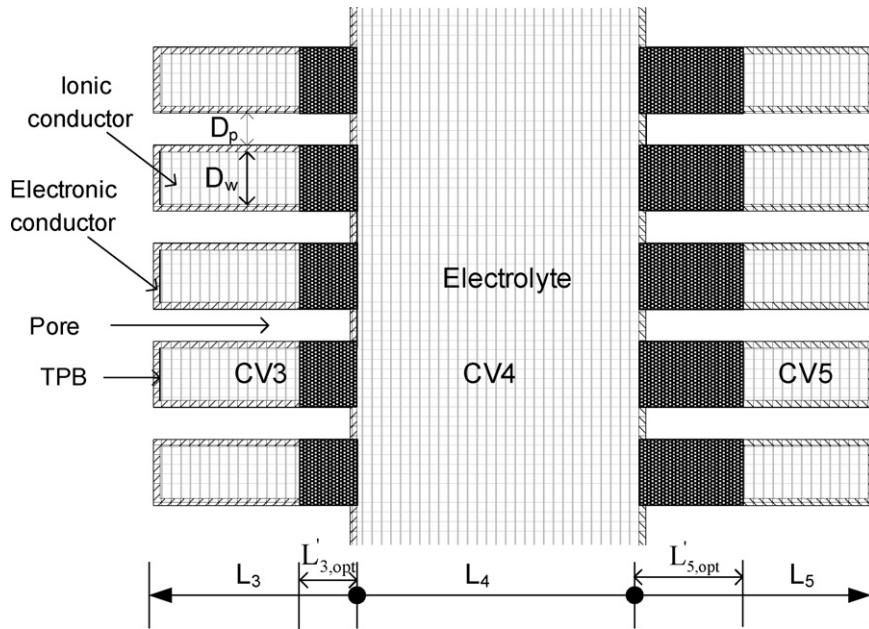


Fig. 2. Model of the positive electrode–electrolyte–negative electrode assembly (PEN) internal structure with the composite electrodes.

$$D_5 = \frac{1.43 \times 10^{-7} T_5^{1.75} (M_{O_2} + M_{N_2})^{1/2}}{P_{\text{air}} (2M_{O_2} M_{N_2})^{1/2} (\nu_{O_2}^{1/3} + \nu_{N_2}^{1/3})^2} \quad (22b)$$

where ν is the diffusion volume of simple molecules.

Therefore, for CV3, the energy balance accounts for energy change due to the heat transfer, potential losses heating, mass transfer, and the heat generated during the electrochemical reaction, as follows:

$$\frac{d\theta_3}{d\tau} = \frac{[-\tilde{Q}_{\text{rad},1-3} - \tilde{Q}_{\text{cnv},2-3} + \tilde{Q}_{\text{ohm},3} + \tilde{Q}_{\text{actconc},3} + \tilde{Q}_{\text{cnd},3-4} - \tilde{Q}_{\text{cnd},1-3} + \tilde{Q}_{\text{mass},3} + \alpha \tilde{Q}_{\text{rct}}]}{\tilde{N}_3} \quad (23)$$

where $\tilde{Q}_{\text{cnd},3-4}$ is the dimensionless heat conduction from the electrolyte to the anode layer, and it is given by:

$$\tilde{Q}_{\text{cnd},3-4} = \frac{2\tilde{k}_3\tilde{k}_4\tilde{A}_{\text{cnd},3-4}(\theta_4 - \theta_3)}{\xi_4\tilde{k}_3 + \xi_3\tilde{k}_4} \quad (24)$$

The effective heat conduction area, $\tilde{A}_{\text{cnd},3-4}$, in Eq. (24) is given by. $\tilde{A}_{\text{cnd},3-4} = (1 - \phi_3)\xi_y\xi_z$ Besides, $\tilde{Q}_{\text{mass},3}$, the energy change of CV3 due to the mass flow across its boundaries, is given by:

$$\tilde{Q}_{\text{mass},3} = \frac{\dot{n}_{H_2}(H_{H_2,2} - H_{H_2,3}) + \dot{n}_{H_2O}(H_{H_2O,4} - H_{H_2O,3})}{\dot{m}_{\text{ref}}c_{p,f}T_{\text{ref}}} \quad (25)$$

The energy equation for CV4, based on the first law of thermodynamics, is written as follows:

$$\frac{d\theta_4}{d\tau} = \frac{[-\tilde{Q}_{\text{cnd},3-4} + \tilde{Q}_{\text{cnd},4-5} + \tilde{Q}_{\text{ohm},4} + \tilde{Q}_{\text{mass},4}]}{\tilde{N}_4} \quad (26)$$

The dimensionless heat conduction rate from the cathode layer to the electrolyte is written as:

$$\tilde{Q}_{\text{cnd},4-5} = \frac{2\tilde{k}_4\tilde{k}_5\tilde{A}_{\text{cnd},4-5}(\theta_5 - \theta_4)}{\xi_5\tilde{k}_4 + \xi_4\tilde{k}_5} \quad (27)$$

where the effective conduction heat transfer area is $\tilde{A}_{\text{cnd},4-5} = (1 - \phi_5)\xi_y\xi_z$.

The energy change due to mass transfer across the electrolyte boundaries is calculated as:

$$\tilde{Q}_{\text{mass},4} = \frac{\dot{n}_{H_2}(H_{H_2,3} - H_{H_2,4}) + \dot{n}_{O_2}(H_{O_2,5} - H_{O_2,4})}{\dot{m}_{\text{ref}}c_{p,f}T_{\text{ref}}} \quad (28)$$

Similarly to the anode layer, the transient variation of the cathode layer temperature is obtained based on the first law of thermodynamics as follows:

$$\frac{d\theta_5}{d\tau} = \frac{[-\tilde{Q}_{\text{rad},1-5} + \tilde{Q}_{\text{cnv},5-6} + \tilde{Q}_{\text{ohm},5} + \tilde{Q}_{\text{actconc},5} - \tilde{Q}_{\text{cnd},4-5} - \tilde{Q}_{\text{cnd},1-5} + \tilde{Q}_{\text{mass},5} + (1 - \alpha)\tilde{Q}_{\text{rct}}]}{\tilde{N}_5} \quad (29)$$

where the dimensionless convective heat transfer rate from the oxidant channels to the cathode layer is:

$$\tilde{Q}_{\text{cnv},5-6} = \tilde{h}_6 n_{\text{ch}} \xi_{\text{ch}} \xi_z (1 - \phi_5)(\theta_6 - \theta_5) \quad (30)$$

And the energy change due to mass transfer across the cathode layer boundaries is:

$$\tilde{Q}_{\text{mass},5} = \frac{\dot{n}_{O_2}(H_{O_2,6} - H_{O_2,5}) + \dot{n}_{O_2}(X_{N_2}/X_{O_2})(H_{N_2,6} - H_{N_2,5})}{\dot{m}_{\text{ref}}c_{p,f}T_{\text{ref}}} \quad (31)$$

The energy balance in the oxidant channels in CV6 yields:

$$\frac{d\theta_6}{d\tau} = \frac{[-\tilde{Q}_{\text{cnv},1-6} - \tilde{Q}_{\text{cnv},5-6} + \tilde{Q}_{\text{mass},6}]}{\tilde{N}_6} \quad (32)$$

where the energy change due to mass transfer across the oxidant channels boundaries is:

$$\tilde{Q}_{\text{mass},6} = \frac{\dot{n}_{O_2,\text{in}}(H_{O_2,\text{air}} - H_{O_2,6}) + \dot{n}_{N_2,\text{in}}(H_{N_2,\text{air}} - H_{N_2,6})}{\dot{m}_{\text{ref}}c_{p,f}T_{\text{ref}}} \quad (33)$$

The dimensionless heat capacity of CV6 is given by:

$$\tilde{N}_6 = \frac{P_{\text{air}} n_{\text{ch}} L_{\text{ch}} L_6 L_z (X_{O_2} c_{v,O_2} + X_{N_2} c_{v,N_2})}{RT_6 \dot{m}_{\text{ref}} c_{p,f}} \quad (34)$$

The pumping power needed to supply fuel and oxidant to the single cell are calculated based on the assumption that the pumping

process is adiabatic:

$$W_P = \dot{m}_2 \frac{\kappa_2}{\kappa_2 - 1} R_2 T_2 \left[\left(\frac{p_f + \Delta p_2}{p_f} \right)^{(\kappa_2 - 1)/\kappa_2} - 1 \right] + \dot{m}_6 \frac{\kappa_6}{\kappa_6 - 1} R_6 T_6 \left[\left(\frac{p_{\text{air}} + \Delta p_6}{p_{\text{air}}} \right)^{(\kappa_6 - 1)/\kappa_6} - 1 \right] \quad (35)$$

where the pressure drop in the fuel channels and oxidant channels are:

$$\Delta p_2 = \frac{2f_2 L_y \rho_2 u_2^2}{D_{h,2}}, \quad \Delta p_6 = \frac{2f_6 L_z \rho_6 u_6^2}{D_{h,6}} \quad (36)$$

The average mass flow rates in the fuel and oxidant channels are given by:

$$\dot{m}_2 = \frac{1}{2} [M_{\text{H}_2}(\dot{n}_{\text{H}_2,\text{in}} + \dot{n}_{\text{H}_2,\text{out}}) + M_{\text{H}_2\text{O}}\dot{n}_{\text{H}_2\text{O}}] \quad (37a)$$

$$\dot{m}_6 = \frac{1}{2} [M_{\text{O}_2}(\dot{n}_{\text{O}_2,\text{in}} + \dot{n}_{\text{O}_2,\text{out}}) + M_{\text{N}_2}(\dot{n}_{\text{N}_2,\text{in}} + \dot{n}_{\text{N}_2,\text{out}})] \quad (37b)$$

In Eq. (35), κ_j is the isentropic index and given as $\kappa_j = c_{p,j}/c_{v,j}$, $j = 2, 6$. R_j is the specific gas constant and calculated by $R_j = c_{p,j} - c_{v,j}$. Note that the subscript j here indicates the gas mixture in the fuel and oxidant channels.

3. Electrochemical model

To complete the model of the single SOFC, the thermal model needs to be coupled with the electrochemical counterpart before the SOFC performance can be evaluated.

The actual operating potential of the single SOFC, V , is derived from the open circuit potential, V_{ocp} , by taking into account various kinds of losses, i.e., the activation losses and the concentration losses in the anode layer and cathode layer, $\eta_{\text{act},j}$ and $\eta_{\text{conc},j}$, as well as the ohmic losses in all the solid compartments of the fuel cell, $\eta_{\text{ohm},j}$:

$$V = V_{\text{ocp}} - \left(\sum_j \eta_{\text{ohm},j} + \eta_{\text{conc},3} + \eta_{\text{conc},5} + \eta_{\text{act},3} + \eta_{\text{act},5} \right), \quad j = 1, 3, 4, 5 \quad (38)$$

where the open circuit potential, V_{ocp} , is estimated by the difference of Gibbs free energy between the reactants and products of the electrochemical reactions described by Eqs. (1) and (2). Its calculation is reported by Kim et al. [18] based on the assumption that both reactions occur at the electrolyte temperature, T_4 :

$$V_{\text{ocp}} = \frac{-(H_{\text{H}_2\text{O},4} - H_{\text{H}_2,4} - 1/2H_{\text{O}_2,4}) - T_4(S_{\text{H}_2\text{O},4}^0 - S_{\text{H}_2,4}^0 - 1/2S_{\text{O}_2,4}^0) + RT_4 \ln[P_{\text{H}_2\text{O}}/(P_{\text{H}_2}(P_{\text{O}_2})^{1/2})]}{2F} \quad (39)$$

The total potential losses in each electrode, $\eta_{\text{total},j}$, is defined as:

$$\eta_{\text{total},j} = \eta_{\text{act},j} + \eta_{\text{ohm},j} + \eta_{\text{conc},j}, \quad j = 3, 5 \quad (40)$$

The composite electrodes of the single SOFC are a mixture of electronic and ionic conductor (electrolyte material). In the present study, the electrolyte material in the composite electrodes is modeled as regularly spaced corrugations, which protrude from the dense electrolyte surface, as shown in Fig. 2. The electronic conducting material is spread over the electrolyte material. The remaining space corresponds to parallel tube-like pores for the transport of gaseous species [21]. The interface of the ionic conductor, electronic conductor and reacting gases is called three-phase boundary (TPB), and corresponds to the sites where the electrochemical reaction could take place. The active TPB regions, $L'_{j,\text{opt}}$, refer to the TPB sites where the electrochemical reactions actually occur. According to Chan and Xia [22], the electrochemical reactions take place

where the total potential losses in each electrode, $\eta_{\text{total},j}$, reach a minimum.

The ohmic loss, $\eta_{\text{ohm},j}$, is obtained based on the Ohm's law as follows:

$$\eta_{\text{ohm},j} = I\beta_j, \quad j = 1, 4 \quad (41a)$$

$$\eta_{\text{ohm},j} = \frac{I(A'_{j,\text{opt}} - L_y L_z)L'_{j,\text{opt}}}{2A'_{j,\text{opt}}L_y L_z(1 - \phi_j)\sigma_4} + \frac{I(L_j - L'_{j,\text{opt}})}{L_y L_z(1 - 1.8\phi_j)\sigma_j}, \quad j = 3, 5 \quad (41b)$$

where the electrical resistances of the interconnect and electrolyte, β_1 and β_4 , are calculated according to their material and geometric features as follows [1]:

$$\beta_1 = \frac{L_1}{L_y L_z \sigma_1} + \frac{L_2}{(1 + n_{\text{ch}})L_t L_y \sigma_1} + \frac{L_6}{(1 + n_{\text{ch}})L_t L_z \sigma_1} \quad (42a)$$

$$\beta_4 = \frac{L_4}{L_y L_z \sigma_4} \quad (42b)$$

where σ_j is the electrical conductivity of each control volume.

The first term at the right side of Eq. (41b) accounts for the ohmic losses in the active TPB regions where the ionic conducting resistance is dominant, the second term refers to the remaining regions of the electrodes where only electronic conducting resistance exists. $A'_{j,\text{opt}}$ refers to the area of the active TPB regions in each electrode, and it is calculated with $A'_{j,\text{opt}} = (1 + 2L'_{j,\text{opt}}\phi_j/D_{p,j})L_y L_z$. Here, $D_{p,j}$ stands for the average diameter of the parallel pores in the electrodes and it is obtained with $D_{p,j} = D_{w,j}\phi_j/(1 - \phi_j)$. $D_{w,j}$ is the width of a corrugation with electrolyte material as shown in Fig. 2 and its value is given by Tanner et al. [21].

When electrochemical reactions take place rapidly, the concentrations of reactants at the reacting region drop, which result in the so-called concentration losses. The working current densities at which the fuel concentration and the oxidant concentration decrease to 0 are defined as the anode and cathode limiting current densities, i_{as} and i_{cs} , respectively. Based on the TPB pressure correlation given by Eq. (21), the limiting current densities are written as:

$$i_{\text{as}} = \frac{2FX_{\text{H}_2}p_{\text{air}}D_3\phi_3}{RT_3\psi_3L_3} \quad (43a)$$

$$i_{\text{cs}} = \frac{4FD_5\phi_5p_{\text{air}}}{RT_5\psi_5L_5} \ln \left(\frac{p_{\text{air}}}{p_{\text{air}} - X_{\text{O}_2}p_{\text{air}}} \right) \quad (43b)$$

The concentration overpotentials in the anode layer and cathode layer are given by Aguiar et al. [19] as:

$$\eta_{\text{conc},c} = \frac{RT_5}{4F} \ln \left(\frac{P_{\text{O}_2}}{P_{\text{O}_2,\text{TPB}}} \right) \quad (44a)$$

$$\eta_{\text{conc},a} = \frac{RT_3}{2F} \ln \left(\frac{P_{\text{H}_2}P_{\text{H}_2\text{O},\text{TPB}}}{P_{\text{H}_2,\text{TPB}}P_{\text{H}_2\text{O}}} \right) \quad (44b)$$

The activation losses, $\eta_{\text{act},j}$, represent the energy needed to activate electrochemical reactions. In the present study they are estimated by the Butler–Volmer equation [23] as follows:

$$i_j = i_{0,j} \left[\exp \left(\frac{\alpha_c n F}{RT_j} \eta_{\text{act},j} \right) - \exp \left(-\frac{(1 - \alpha_c) n F}{RT_j} \eta_{\text{act},j} \right) \right], \quad j = 3, 5 \quad (45)$$

In Eq. (45) n takes the value of 2, α_c stands for the charge transfer coefficient, and when it takes the typical value of 0.5, the explicit form of Eq. (45) for the activation overpotentials is given by:

$$\eta_{act,j} = \frac{RT_j}{\alpha_c n F} \sinh^{-1} \left(\frac{i_j}{2i_{0,j}} \right), \quad j = 3, 5 \quad (46)$$

where $i_{0,j}$ stands for the exchange current densities and are reported by Aguiar et al. [19] as follows:

$$i_{0,j} = \frac{RT_j}{nF} \delta_j \exp \left(-\frac{E_j}{RT_j} \right), \quad j = 3, 5 \quad (47)$$

where δ_j and E_j are the pre-exponential factor and the activation energy, respectively. Their values are reported by Aguiar et al. [19].

In Eq. (46), the working current densities at both electrodes, i_j , are defined as $i_j = I/A'_{j,opt}$.

With the knowledge of actual operating potential calculated by Eq. (38), the electrical power of the single SOFC is obtained with:

$$W_E = VI \quad (48)$$

And the net power (available for utilization) of the single SOFC is derived from its electrical power by subtracting the required pumping power:

$$W_N = W_E - W_P \quad (49)$$

The working current and calculated potentials and powers from the model are then nondimensionalized as follows:

$$\tilde{I} = \frac{I}{I_{ref}} \quad (50)$$

where I_{ref} is a specified reference current and \tilde{I} is the dimensionless current.

$$\tilde{V}_j = \frac{V_j}{V_{ref}}, \quad \tilde{\eta}_j = \frac{\eta_j}{V_{ref}} \quad (51)$$

where $V_{ref} = (\dot{m}_{ref} c_{p,f} T_{ref})/I_{ref}$ stands for the reference voltage. \tilde{V} and $\tilde{\eta}$ are the dimensionless potential and potential losses, respectively. Subscript j denotes all the potentials and potential losses present in the fuel cell.

$$\tilde{W}_j = \frac{W_j}{W_{ref}}, \quad j = E, P, N \quad (52)$$

where W_{ref} is the reference power defined as $W_{ref} = \dot{m}_{ref} c_{p,f} T_{ref} \tilde{W}$ is the dimensionless power.

4. Results and discussion

In an effort to validate the model, we compared the electrochemical performance simulated with the current model with results published by Aguiar et al. [19]. Fig. 3 illustrates such comparison. It can be seen that under same SOFC geometric dimensions and operating condition (1073 K), the general shape of two polarization curves are similar, as well as the relative magnitude between each kind of potential losses. The biggest difference observed is in the ohmic losses. This can be explained from the difference in the modeling of ohmic losses. The main difference is that in the present model: (i) the composite electrodes are a mixture of electronic and ionic conductor with different conductivities; (ii) the charge-transfer reaction happens at the active TPB region expanding a small distance from the electrode/electrolyte interface; (iii) the ionic conducting resistance in the active TPB region is accounted for; (iv) ohmic losses of the interconnect are accounted for in the current model. As a result, the ohmic losses in the present model are slightly larger than the one in Aguiar et al. [19]. However,

Table 1
Properties and constant values used in the simulations.

$B = 5.6697 \times 10^{-8} \text{ W m}^{-2} \text{ K}^{-4}$	$V_T = 3.07 \times 10^{-5} \text{ m}^3$
$c_{p,1} = 0.5 \times 10^3 \text{ J kg}^{-1} \text{ K}^{-1}$	$Zr_3 = Zr_5 = 10^{-6} \text{ m}$
$c_{p,3} = 0.595 \times 10^3 \text{ J kg}^{-1} \text{ K}^{-1}$	$\alpha = 0.5$
$c_{p,4} = 0.606 \times 10^3 \text{ J kg}^{-1} \text{ K}^{-1}$	$\delta_3 = 6.54 \times 10^{11} \Omega^{-1} \text{ m}^{-2}$
$c_{p,5} = 0.573 \times 10^3 \text{ J kg}^{-1} \text{ K}^{-1}$	$\delta_5 = 2.35 \times 10^{11} \Omega^{-1} \text{ m}^{-2}$
$c_{p,f} = 14983 \text{ J kg}^{-1} \text{ K}^{-1}$	$\varepsilon_1 = 0.1$
$c_{v,H_2} = 21.718 \text{ J mol}^{-1} \text{ K}^{-1}$	$\varepsilon_3 = \varepsilon_5 = 0.8$
$c_{v,H_2O} = 33.156 \text{ J mol}^{-1} \text{ K}^{-1}$	$\nu_{O_2} = 16.3 \text{ cm}^3$
$c_{v,O_2} = 26.56 \text{ J mol}^{-1} \text{ K}^{-1}$	$\nu_{N_2} = 18.5 \text{ cm}^3$
$c_{v,N_2} = 24.36 \text{ J mol}^{-1} \text{ K}^{-1}$	$\nu_{H_2} = 6.12 \text{ cm}^3$
$D_{w,3} = 14 \times 10^{-6} \text{ m}$	$\nu_{H_2O} = 13.1 \text{ cm}^3$
$D_{w,5} = 14 \times 10^{-6} \text{ m}$	$\xi_{ch} = 6.4 \times 10^{-2}$
$E_3 = 140 \times 10^3 \text{ J mol}^{-1}$	$\xi_t = 2.56 \times 10^{-1}$
$E_5 = 137 \times 10^3 \text{ J mol}^{-1}$	$\rho_1 = 8000 \text{ kg m}^{-3}$
$F = 96500 \text{ C mol}^{-1}$	$\rho_3 = 6870 \text{ kg m}^{-3}$
$I_{ref} = 116.58 \text{ A}$	$\rho_4 = 5900 \text{ kg m}^{-3}$
$k_f = k_2 = 0.43 \text{ W m}^{-1} \text{ K}^{-1}$	$\rho_5 = 6570 \text{ kg m}^{-3}$
$k_{air} = k_6 = 0.0717 \text{ W m}^{-1} \text{ K}^{-1}$	$\sigma_1 = 1.5 \times 10^6 \Omega^{-1} \text{ m}^{-1}$
$k_1 = 25 \text{ W m}^{-1} \text{ K}^{-1}$	$\sigma_3 = 8.0 \times 10^4 \Omega^{-1} \text{ m}^{-1}$
$k_3 = k_5 = 2 \text{ W m}^{-1} \text{ K}^{-1}$	$\sigma_4 = 33.4 \times 10^3 \exp(-10.3 \times 10^3/T) \Omega^{-1} \text{ m}^{-1}$
$k_4 = 2 \text{ W m}^{-1} \text{ K}^{-1}$	$\sigma_5 = 8.4 \times 10^3 \Omega^{-1} \text{ m}^{-1}$
$n_{ch} = 10$	$\phi_3 = 0.4$
$p_f = p_{air} = 0.1 \text{ MPa}$	$\phi_5 = 0.5$
$p_{ref} = 0.1 \text{ MPa}$	$\psi_3 = 9.5$
$R = 8.314 \text{ J mol}^{-1} \text{ K}^{-1}$	$\psi_5 = 7.2$
$T_{air,in} = 923.15 \text{ K}$	$\mu_f = 2.07 \times 10^{-5} \text{ Pa s}$
$T_{f,in} = 923.15 \text{ K}$	$\mu_{air} = 4.18 \times 10^{-5} \text{ Pa s}$
$T_{ref} = 298.15 \text{ K}$	

the qualitative behavior of both electrochemical models is very similar.

The values of the physical properties utilized to obtain the simulation results shown in this section with the present model are listed in Table 1. The inlet temperature and pressure of both fuel and oxidant are assumed as 923.15 K (T_f, T_{air}) and 1 atm (p_f, p_{air}), respectively. The geometric features of the single SOFC are shown in Fig. 1, which include the external dimensions (L_x, L_y , and L_z), the individual layers thicknesses (L_i), the width (L_{ch}) and shoulder thicknesses (L_t) of fuel and oxidant channels, and the number of channels embedded in the bipolar plate (n_{ch}).

As discussed in the previous section, the thermal model of the single SOFC consists of six dimensionless ordinary differential equations to obtain the temperatures of each CV and three algebraic equations to obtain the partial pressures at the active three-phase boundaries (TPB) regions, i.e., Eqs. (21a)–(21c). The present study focuses on the optimization of SOFC internal structure and operating conditions at steady state to achieve the maximum electrical power output. As a result, only the steady state solutions of the model are considered, which are obtained by making the time derivatives of the temperature for each control volume equal to zero and then solving them with a quasi-Newton method [24]. The contribution of $\dot{Q}_{actconc,j}$ was assumed negligible in Eqs. (23) and (29). Activation and concentration losses still affect the nominal temperature through the actual operating potential Eq. (38). The obtained solutions are then used in the electrochemical model, with which the electrochemical performance of the single SOFC is evaluated.

Fig. 4 shows the way to determine the active TPB region at the anode, $\xi'_{3,opt}$, which in this model corresponds to the reaction layer thickness, ξ'_3 , that minimizes the total potential losses at the anode. Three total anode thicknesses are considered, $\xi_3 = 6.4 \times 10^{-4}$ (dotted line), $\xi_3 = 16 \times 10^{-4}$ (dashed line) and $\xi_3 = 160 \times 10^{-4}$ (solid line) (the dotted and dashed lines overlap). The total potential losses at the anode reach a minimum at $\xi'_{3,opt} = 3.52 \times 10^{-4}$, 3.2×10^{-4} and 2.98×10^{-4} for working currents of $\tilde{I} = 0.172$, 0.344 and 0.516, respectively, regardless of the total anode thickness ξ_3 . The optimal, $\xi'_{3,opt}$, is insensitive to the changes in the anode

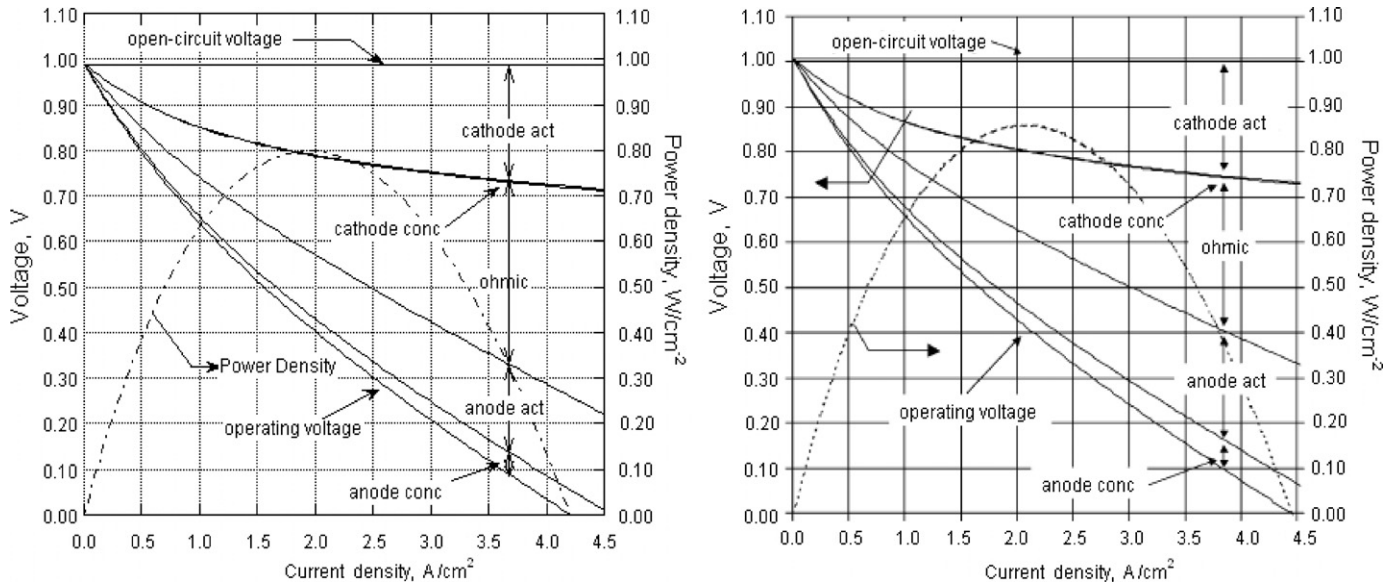


Fig. 3. Comparison of polarization curves and power density simulated in current model (left) and on Aguiar et al. [19] (right).

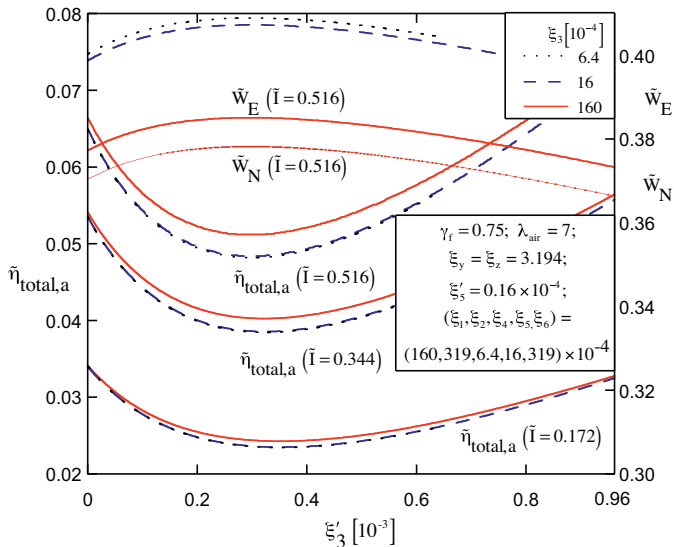


Fig. 4. The total potential losses at the anode and electrical power and net power as functions of anode reaction region thickness under various working currents and anode thickness.

thickness. Fig. 4 also shows that the value of ξ'_3 where the total potential losses in the anode reach a minimum is also the active anode thickness where electrical and net power reach a maximum (e.g., $\xi'_{3,opt} = 2.98 \times 10^{-4}$ for a working current of $\tilde{I} = 0.516$). The electrical power and net power curves are parallel, since for the conditions of Fig. 4, the pumping power is constant for each current level.

Fig. 5 shows the way to determine the active TPB region at the cathode, $\xi'_{5,opt}$. Similar conclusions to the anode side are obtained: the optimal ξ'_5 is practically insensitive to the changes in the cathode thickness; the optimal ξ'_5 where the total potential losses in the cathode reach a minimum is also the optimal ξ'_5 where electrical and net power reach a maximum. When the working currents \tilde{I} are 0.172, 0.344 and 0.516, the active TPB regions at the cathode, $\xi'_{5,opt}$, are 5.19×10^{-4} , 4.61×10^{-4} and 4.13×10^{-4} , respectively. Since the total potential losses at the anode and cathode are computed separately and do not influence each other, $\xi'_{3,opt}$ and $\xi'_{5,opt}$ are independent of each other.

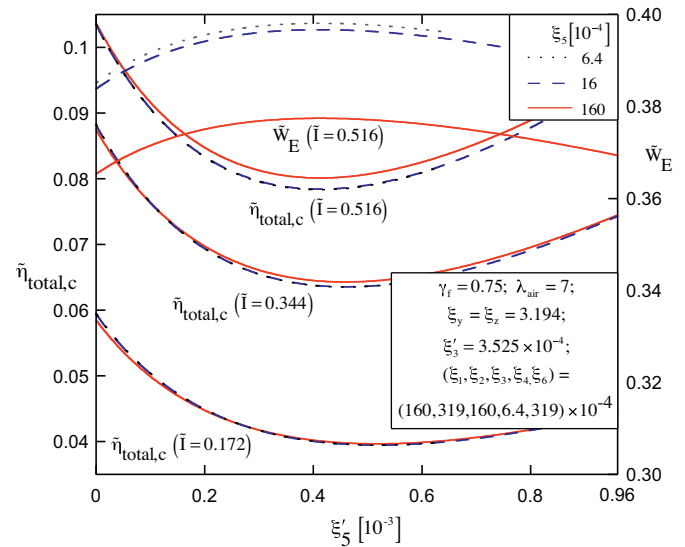


Fig. 5. The total potential losses at the cathode and electrical power as functions of cathode reaction region thickness under various working currents and cathode thicknesses.

Fig. 6 shows the typical temperature profile of each compartment in the single SOFC. It is observed that as the current increases, the temperature of all the control volumes increase as well. The reason is that the higher the current is, the more fuel is consumed in the electrochemical reaction, as a result, more heat is generated in the single SOFC which causes the temperature of all CVs to increase. Fig. 6 also shows that there is significant temperature spatial gradient across each compartment, especially the temperature difference between the oxidant channels (6) and the PEN (3, 4, 5) (positive electrode–electrolyte–negative electrode assembly) in the present model. This is due to the poor thermal conductivity of oxygen compared with hydrogen and the solid materials of the SOFC. The temperature spatial gradient has a direct impact on the fuel cell's performance, therefore the performance evaluation (featured by electrical power and polarization curves) should take all the internal spatial temperature gradients into consideration.

Fig. 7 shows the typical polarization curves of the single SOFC. As the current increases, the temperatures of all the SOFC com-

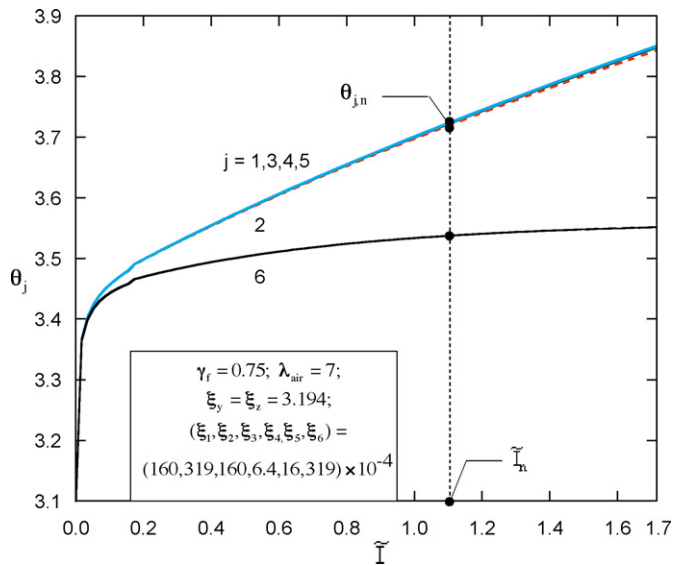


Fig. 6. The temperature of each compartment in the single SOFC as functions of current.

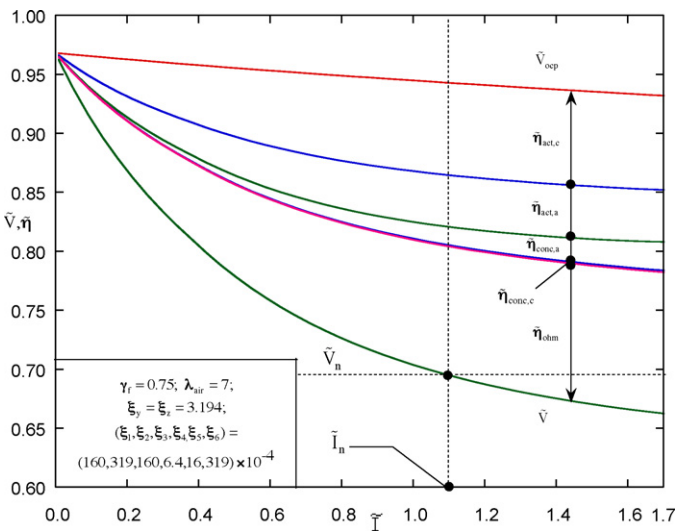


Fig. 7. The polarization curves of the single SOFC.

partments increase. As a result, the Gibbs free energy difference between the reactants and products of the electrochemical reactions decreases, which leads to the drop in open circuit potential according to Eq. (39). In addition, all types of overpotentials, including the activation overpotential, concentration overpotential and ohmic overpotential, increase monotonically as the current increases, which, combined with the decrease of open circuit potential, results in the drop of the actual working potential, according to Eq. (38). Besides, it is observed in Fig. 7 that for small currents, the activation overpotential is dominant among all the potential losses. With the increase of current, the ohmic overpotential grows rapidly.

Fuel cells are normally designed to operate at a cell voltage between 0.6 and 0.7 V [19] and specifically, SOFC systems are presently rated at a cell voltage of 0.7 V per cell [25]. In this study, the nominal operating point is defined as the operating point at which the actual working potential is 0.7 V. From the polarization curves of Fig. 7, the dimensionless working current at the nominal operating point is 1.1, and from Fig. 6, the dimensionless temperature of the PEN at the nominal operating point is about 3.72.

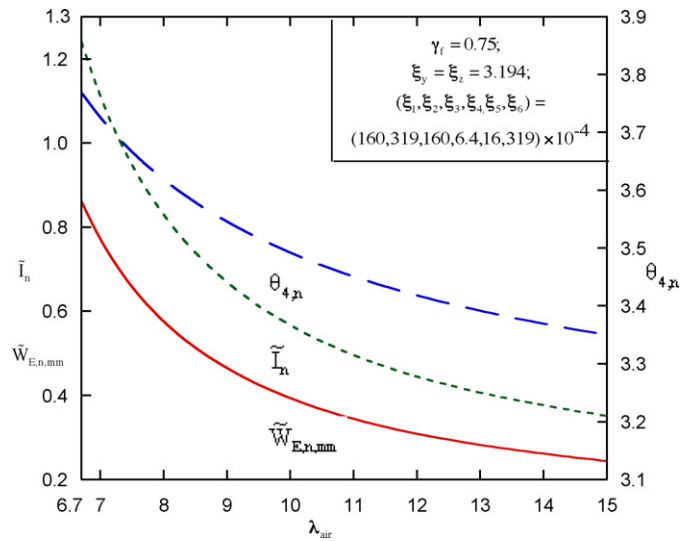


Fig. 8. The working current, electrical power and electrolyte temperature at the nominal operating point as functions of air stoichiometric ratio.

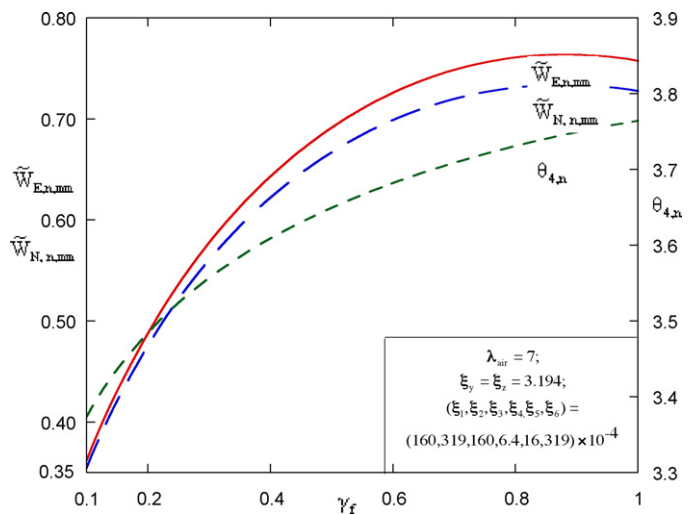


Fig. 9. The electrolyte temperature, electrical power and net power at the nominal operating point as functions of fuel utilization factor.

The effect of air stoichiometric ratio, λ_{air} , on the performance of the single SOFC is illustrated in Fig. 8. It is observed that the nominal current and electrical power decrease as the air stoichiometric ratio increases, which illustrates that large air stoichiometric ratios do not benefit SOFC performance. Such phenomenon can be explained physically: as the air stoichiometric ratio increases, more air with comparably low temperature flows through the oxidant channels, which leads to the drop in SOFC temperature, as shown in Fig. 8. As the temperature of the single SOFC decreases, the total potential losses increase rapidly and the actual working potential drops, ending up with small current and low electrical power at the nominal operating point.

Fig. 9 illustrates the significant impact that the fuel utilization factor has on the performance of the single SOFC. The maximum dimensionless nominal electrical power reaches 0.765 when $\gamma_f = 0.88$, which is approximately 110% higher than the nominal electrical power of 0.362 when $\gamma_f = 0.1$. Fig. 9 also shows that very large or very small fuel utilization factor does not benefit the SOFC performance. This effect can be explained physically by analyzing two extremes: (i) for large fuel utilization factor, the potential losses decrease due to the relatively high temperature in SOFC (less fuel

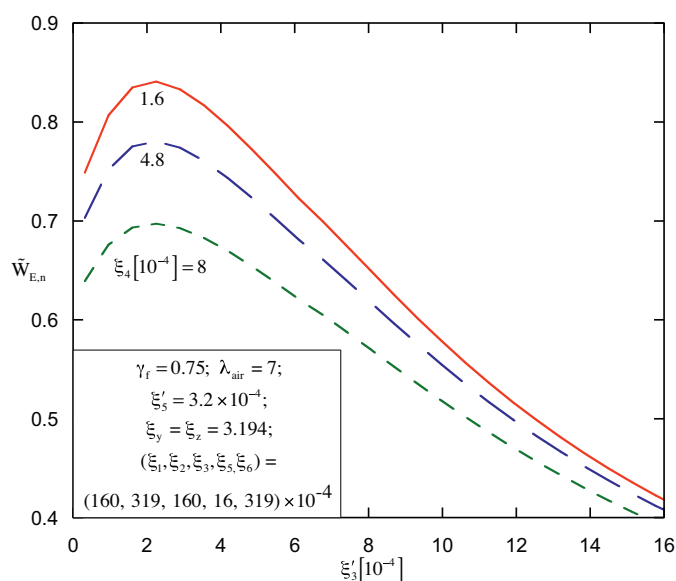


Fig. 10. The electrical power at the nominal operating point as a function of anode reaction region thickness for various electrolyte thicknesses.

with comparably low temperature at inlet flows through the fuel cell), as shown in Fig. 9, however, due to the low concentration of hydrogen in the fuel channels, the open circuit potential also decreases according to Eq. (39), which leads to the drop of actual working potential and ends up with small nominal current and electrical power; (ii) for small fuel utilization factor, the open circuit potential increases (due to the high concentration of hydrogen in the fuel channels), but the potential losses become large due to the low temperature in the fuel cell (more fuel with comparably low temperature at inlet flows through the single SOFC), so the actual working potential decreases at this extreme too, which leads to the low nominal current and electrical power.

Under a constrained operating condition (fixed fuel utilization factor and air stoichiometric ratio), the optimization problem of the PEN internal structure consists of pursuing maximum nominal current and electrical power by optimizing the thickness of the anode, electrolyte and cathode layers subject to a fixed total thickness of PEN, i.e., $L_3 + L_4 + L_5 = \text{constant}$. Note that, for most single SOFCs produced currently, the minimum thickness of the anode, electrolyte and cathode layers are 50 μm , 5 μm and 50 μm , respectively, due to the limitation of manufacturing techniques. The analysis and discussion about the PEN internal structure in this paper is based on a more extended range, and the conclusion from it could be used as reference in the future. The thickness ranges of the anode layer, electrolyte and cathode layer are 5–560 μm , 5–30 μm and 5–560 μm , respectively, and $L_3 + L_4 + L_5 = 570 \mu\text{m}$ ($\xi_3 + \xi_4 + \xi_5 = 182.4 \times 10^{-4}$).

Fig. 10 shows that under a fixed operating condition, $\xi'_{3,opt}$, i.e., the optimal ξ'_3 in which the nominal electrical power reaches a maximum, is robust with respect to changes in electrolyte thickness: $\xi'_{3,opt}$ is 2.399×10^{-4} , 2.415×10^{-4} and 2.431×10^{-4} when ξ_4 is 1.6×10^{-4} , 4.8×10^{-4} and 8×10^{-4} , respectively. With the same method the effect of electrolyte thickness on $\xi'_{5,opt}$ is obtained: $\xi'_{5,opt}$ is 2.822×10^{-4} , 3.129×10^{-4} and 3.332×10^{-4} when ξ_4 is 1.6×10^{-4} , 4.8×10^{-4} and 8×10^{-4} .

Fig. 11 shows how $\xi'_{3,opt}$ and $\xi'_{5,opt}$ change as the electrolyte thickness varies. It is shown that with the selected thickness range of electrolyte, the active TPB region at the cathode, $\xi'_{5,opt}$, is larger than the counterpart at the anode; as the electrolyte increases, both $\xi'_{3,opt}$ and $\xi'_{5,opt}$ increase, though $\xi'_{3,opt}$ is practically insensitive (i.e., robust) with respect to electrolyte thickness variation. The

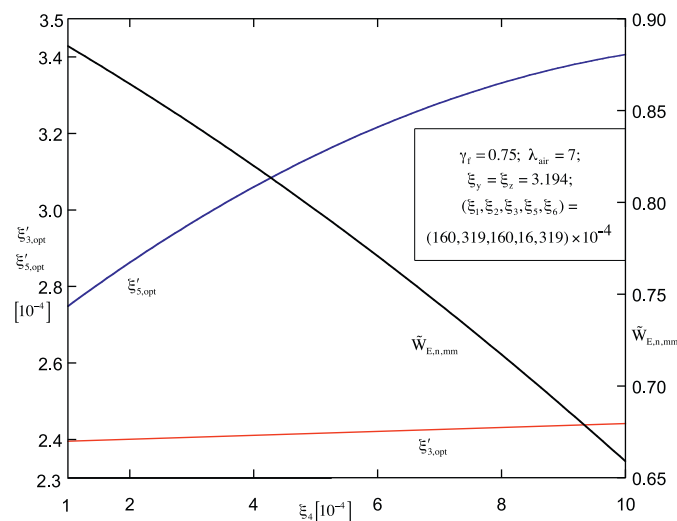


Fig. 11. The active reaction region thickness at the anode and cathode and the two-way maximized electrical power at the nominal operating point as functions of electrolyte thickness.

results of Fig. 11 are used in the next discussion to set the values of $\xi'_{3,opt}$ and $\xi'_{5,opt}$. The two-way maximized electrical power at the nominal operating point is also reported in Fig. 11.

Fig. 12 illustrates the impact of thickness distribution between two electrodes on the performance of the single SOFC, when the electrolyte thickness is fixed. For different electrolyte thicknesses, the nominal electrical power increases as the anode increases at first, and then starts to drop after the anode thickness increases to an optimal value. The optimal thickness distribution between two electrodes is determined by the trade-off between the potential losses at the anode and cathode: (i) for small anode and large cathode, the potential losses at the anode, primarily the concentration losses, would decrease, but the potential losses at the cathode would increase, mainly the ohmic losses; therefore, the total potential losses of the SOFC would increase, which leads to the drop of nominal electrical power; (ii) for the large anode and small cathode, the potential losses at the cathode would decrease, especially the ohmic losses, but the potential losses at the anode, mainly the concentration losses, would increase. In this way, the total potential losses of the SOFC would increase at this extreme too, leading to a drop of nominal electrical power.

Fig. 13 shows the optimal thickness distribution between the anode and cathode as a function of electrolyte thickness under a fixed operating condition. With the selected thickness range of electrolyte, $\xi'_{3,opt}$ is much larger than $\xi'_{5,opt}$, which suggests that under the fixed operating condition, an anode-supported SOFC would perform better than a cathode-supported SOFC. Fig. 13 also shows that optimal anode and cathode thicknesses are essentially unchanged by variations in the electrolyte thickness. As the electrolyte thickness increases, the optimal anode thickness increases slightly and becomes stable when the electrolyte is larger than 8×10^{-4} . The opposite trend is observed for the optimal cathode thickness: as the electrolyte grows, the optimal cathode thickness decreases to some extent at first and becomes stable when the electrolyte is larger than 8×10^{-4} . These observations corroborate the robustness of the optimal internal structure.

Fig. 13 also shows the important impact the electrolyte has on the performance of the single SOFC. Under the fixed operating condition, for the optimal electrode thicknesses distribution and the optimal active reaction region thickness, the three-way maximized nominal electrical power drops sharply as the electrolyte thickness increases, due to its large ionic-conducting resistance and the

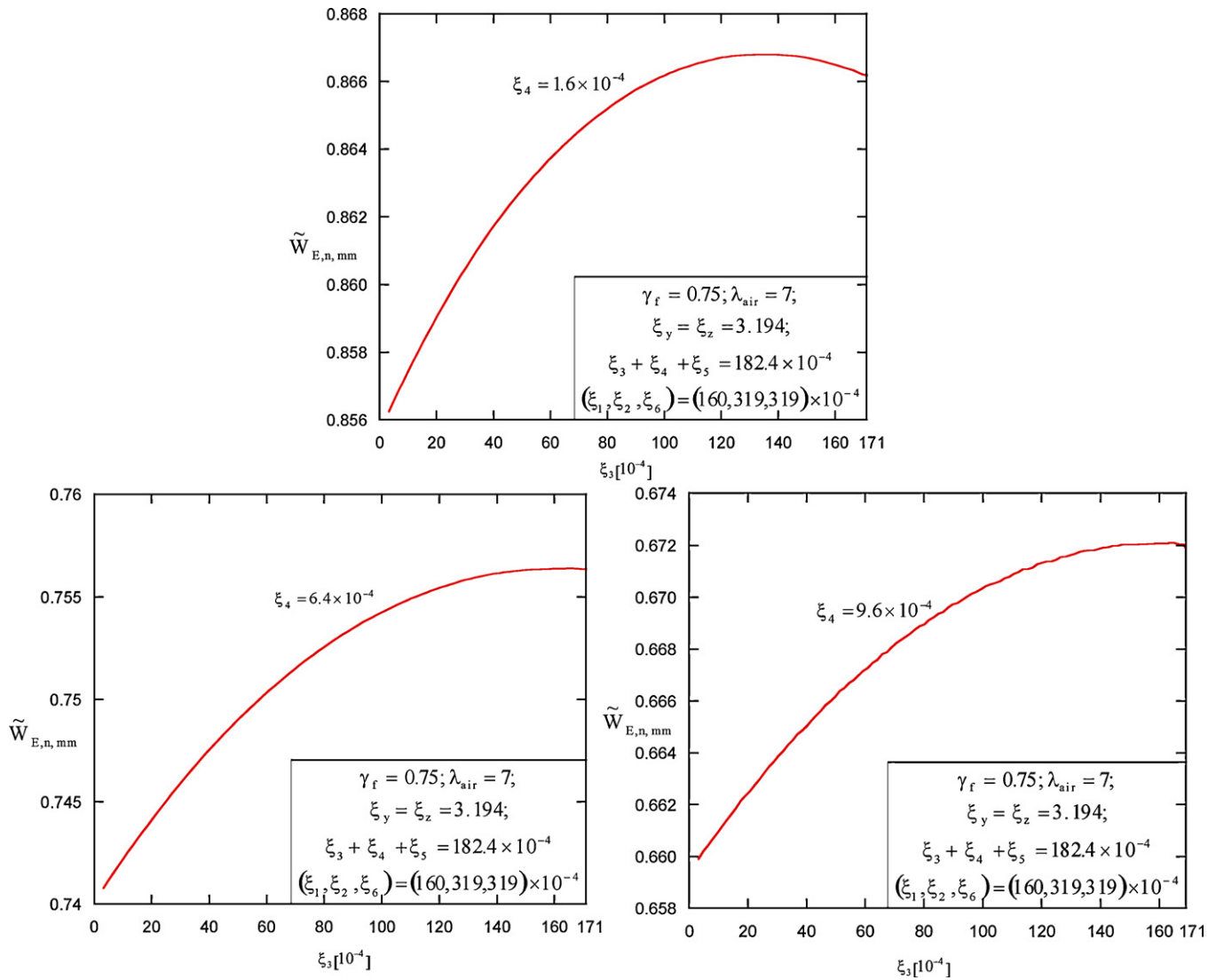


Fig. 12. The two-way maximized electrical power at the nominal operating point as a function of anode layer thickness under various electrolyte thicknesses.

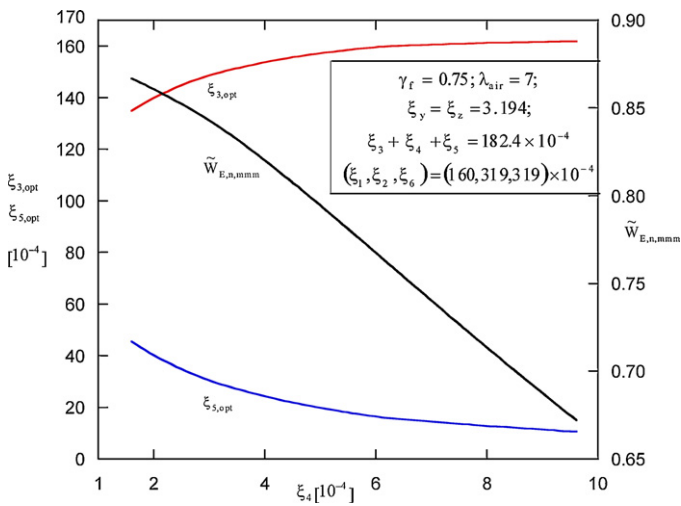


Fig. 13. The optimal thickness distribution between the anode and cathode as well as the three-way maximized electrical power at the nominal operating point as functions of electrolyte thickness.

resulting large ohmic losses. Therefore, the improvement of the ionic-conductivity of the electrolyte and the decrease of its thickness are key issues to improve SOFC performance.

So far, the internal structure optimization has been pursued at fixed operating conditions (i.e., $\gamma_f=0.75$, $\lambda_{air}=7$). In the remaining part of this study, the assumption of constant fuel utilization factor is relaxed. In practice, since the minimum thickness of the electrolyte is determined by the manufacturing techniques, the optimization problem is simplified as follows: for a fixed electrolyte thickness and given total PEN thickness, the optimal thickness distribution between the anode and cathode is pursued to achieve the maximum nominal electrical power. The four degrees of freedom are then the thickness of the active reaction layer region in the anode and cathode, the anode and cathode thickness distribution, and the fuel utilization factor.

Fig. 14 shows how the nominal electrical power changes with the thickness of anode reaction region under various fuel utilization factors. $\xi_{3,opt}$, the optimal ξ'_3 where the nominal electrical power reaches maximum, changes slightly for different fuel utilization factors: $\xi'_{3,opt}$ is 3.11×10^{-4} , 2.59×10^{-4} and 2.39×10^{-4} for $\gamma_f=0.1$, 0.5 and 0.9, respectively. Similarly, for the cathode side, $\xi'_{5,opt}$ is 3.18×10^{-4} , 3.22×10^{-4} and 3.26×10^{-4} for $\gamma_f=0.1$, 0.5 and 0.9, respectively.

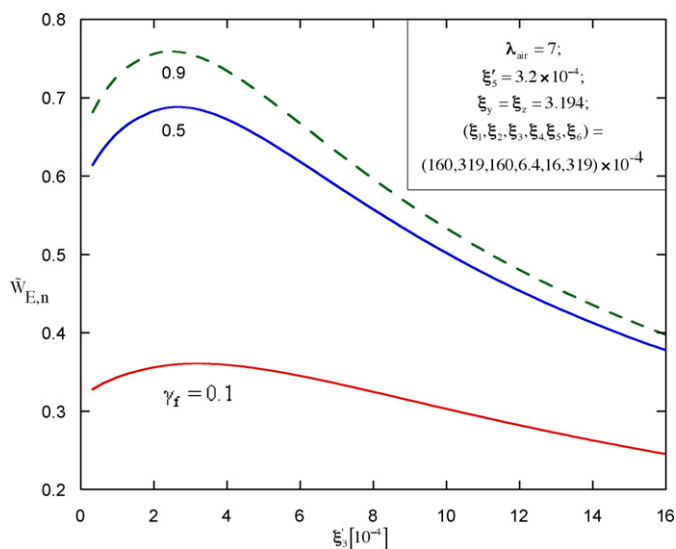


Fig. 14. The electrical power at the nominal operating point as a function of anode reaction region thickness under various fuel utilization factors.

Fig. 15 shows how $\xi'_{3,opt}$ and $\xi'_{5,opt}$ change as the fuel utilization factor varies: as the fuel utilization factor increases, the active reaction region at the anode decreases, whereas the active reaction region at the cathode increases slightly. The results in Fig. 15 are used in the next discussion to set the values of $\xi'_{3,opt}$ and $\xi'_{5,opt}$ as functions of the fuel utilization factor.

Fig. 16 shows how the two-way maximized nominal electrical power (e.g., corresponding to $\xi'_{3,opt}$ and $\xi'_{5,opt}$) changes with fuel utilization factor for different thickness distributions between the two electrodes. The optimal fuel utilization factor, $\gamma_{f,opt}$, are 0.844, 0.863 and 0.878 when ξ_3 is 1.6×10^{-4} , 64×10^{-4} and 160×10^{-4} , respectively. The resulting relationship between the optimal fuel utilization factor and the thickness distribution between the two electrodes is shown in Fig. 17. It is observed that $\gamma_{f,opt}$, the optimal fuel utilization factor, increases as the anode layer thickness increases.

Since $\xi'_{3,opt}$ and $\xi'_{5,opt}$ are functions of the fuel utilization factor (Fig. 15) and the optimal fuel utilization factor is a function of the thickness distribution between the two electrodes (Fig. 17), then $\xi'_{3,opt}$ and $\xi'_{5,opt}$ are functions of the thickness distribution

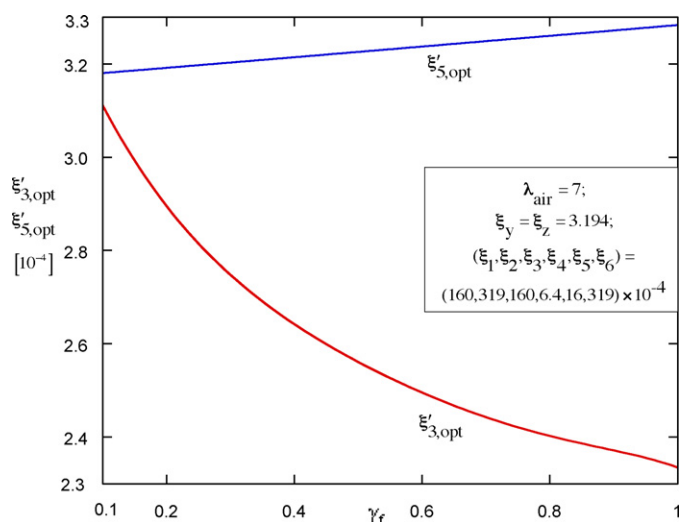


Fig. 15. The active reaction region thicknesses at the anode and cathode as functions of fuel utilization factor.

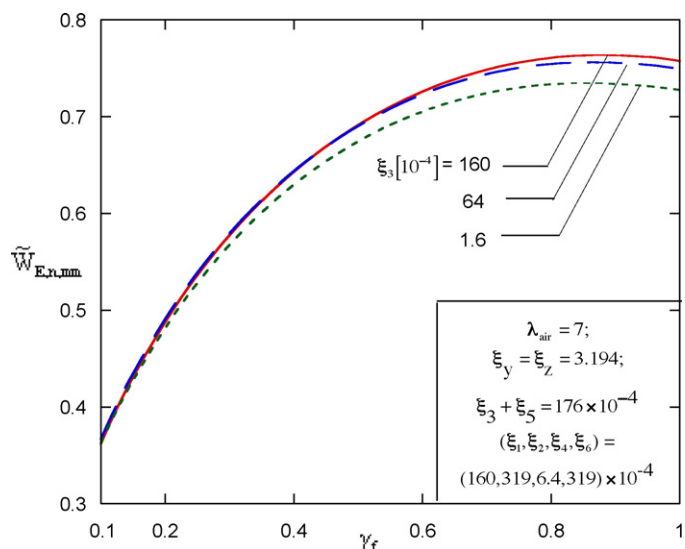


Fig. 16. The two-way maximized electrical power at the nominal operating point as a function of fuel utilization factor for various anode layer thicknesses.

between two electrodes under optimal fuel utilization factor. This relationship is shown in Fig. 18.

The combination of Figs. 17 and 18 shows that as the anode layer thickness increases, the optimal fuel utilization factor increases as well, and accordingly, $\xi'_{3,opt}$, the active TPB region at the anode, decreases slightly, and, $\xi'_{5,opt}$, the active TPB region at cathode increases slightly.

The three-way maximized nominal electrical power as a function of the thickness distribution between the two electrodes is shown in Fig. 17. With the selected thickness range of anode, the $\tilde{W}_{E,n,mmm}$ increases as the anode thickness increases, which means that under flexible operating conditions, the anode-supported SOFC exhibits better performance than the cathode-supported SOFC, when all other parameters are the same.

It is important to note that in the present study, the properties were evaluated at a representative temperature and treated as constants (see Table 1). The properties dependence on temperature can be accounted by introducing appropriate empirical correlations. To quantify the sensitivity with respect to temperature of the parameters shown in Table 1 and their effect on the simulation results,

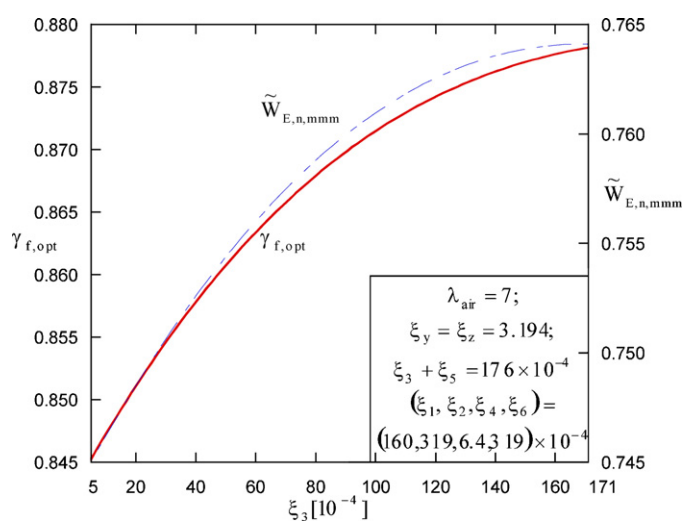


Fig. 17. The optimal fuel utilization factor and three-way maximized electrical power at the nominal operating point as functions of anode layer thickness.

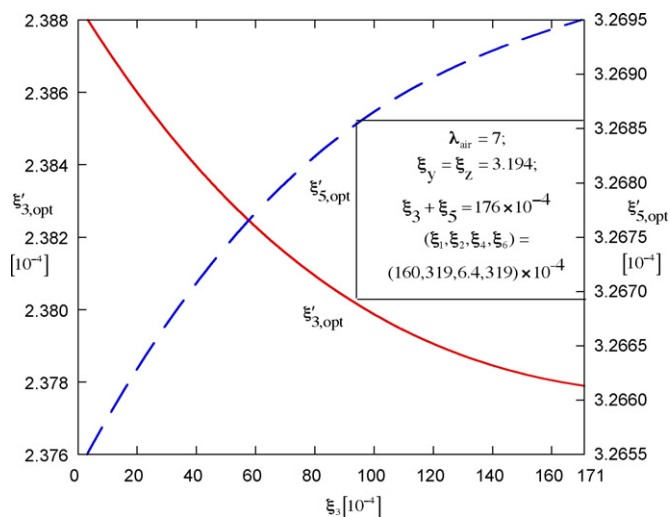


Fig. 18. The active reaction region thicknesses at the anode and cathode as functions of anode layer thickness.

an operating range of 1000–1143 K was selected. In that range, the heat capacities vary by 4%, the thermal conductivity of fuel and air vary by 10.8% and their viscosity by 9%. The corresponding impact in the active TPB thickness at both electrodes is less than 1%. The variation of each control volume temperature is less than 0.5%. The activation overpotential displays a variation of 4.8%, the ohmic overpotential varies by 2.5% and the concentration overpotential by 2.2%.

The temperature profile of the SOFC, the polarization curves and the active TPB at both electrodes are the foundation for the optimization of internal configuration and operating condition. The above discussion shows that the maximum variation observed was less than 5%. This leads to conclude that assuming constant thermal properties in the given operating range is acceptable. This is consistent with a comment by Bove and Ubertini [11].

5. Conclusions

In this paper several important parameters related to the SOFC performance are identified: the internal structure of the positive electrode–electrolyte–negative electrode assembly (PEN), which includes the active TPB regions at the anode and cathode, and the operating condition (fuel utilization factor and air stoichiometric ratio). The analysis of their effects on the SOFC performance is conducted based on a numerical model which accounts for both the thermal and the electrochemical aspects of the single SOFC. The model takes into account relevant aspects concerning fluid flow, mass balance, heat and mass transfer, energy conservation, electrochemical reactions, and takes spatial temperature and pressure gradients into consideration.

The optimization of PEN internal structure includes the optimal thickness allocation between the anode, the electrolyte and the cathode so that several effects such as the open circuit potential and all kinds of losses are appropriately balanced to achieve maximum nominal electrical power. The procedure also addresses the determination of optimal active TPB regions in the electrodes, which is based on the trade-offs between all the potential losses in the electrodes. The active TPB thickness at the anode obtained with the present model is in the range 7.32–11 μm , and the thickness of

the active TPB at the cathode is in the range 8.82–16.2 μm . Those values are consistent with the reaction zone penetration into the electrode reported in Janardhanan and Deutschmann [12] and Nam and Jeon [26].

The optimization of the fuel utilization factor and air stoichiometric ratio is also based on the balance between the effects of SOFC operating temperature and the fuel and oxidant concentration. The maxima found are sharp and therefore, the corresponding optimal geometric and operating parameters could be used as preliminary rules in practical SOFC design.

The present study shows that trade-offs not only exist, but also serve as the basis on which the optimization of SOFC internal structure and operating condition is implemented. In practice, such trade-offs are different from case to case, therefore, they must be pursued based on models that correspond to real applications. However, the methodology of modeling and optimization presented in this paper is generally applicable and can be extended to the analysis of large and more complex SOFC systems.

Acknowledgements

The authors acknowledge with gratitude support from the Office of Naval Research (ONR) under the Electric Ship Research and Development Consortium (ESRDC) and the Institute for Energy Systems, Economics and Sustainability (IESES) at Florida State University.

References

- [1] M. Sorrentino, C. Pianese, Y.G. Guezennec, J. Power Sources 180 (2008) 380–392.
- [2] A.V. Virkar, J. Chen, C.W. Tanner, J.W. Kim, Solid State Ionics 131 (2000) 189–198.
- [3] S.H. Chan, K.A. Khor, Z.T. Xia, J. Power Sources 93 (2001) 130–140.
- [4] M. Sorrentino, A. Mandourah, T.F. Petersen, Y.G. Guezennec, M.J. Moran, G. Rizzoni, Proceedings of the 2004 ASME International Mechanical Engineering Congress and Exposition, Anaheim, CA, November 13–20, 2004.
- [5] J.V.C. Vargas, J.C. Ordonez, A. Bejan, Int. J. Heat Mass Transf. 47 (2004) 4177–4193.
- [6] L.S. Martins, J.E.F.C. Gardolinski, J.V.C. Vargas, J.C. Ordonez, S.C. Amico, M.M.C. Forte, Appl. Therm. Eng. 29 (2009) 3036–3048.
- [7] J.V.C. Vargas, J.C. Ordonez, A. Bejan, Int. J. Heat Mass Transf. 48 (2005) 4410–4427.
- [8] J.C. Ordonez, S. Chen, J.V.C. Vargas, F.G. Dias, J.E.F.C. Gardolinski, D. Vlassov, Int. J. Energy Res. 31 (2007) 1337–1357.
- [9] J.B. Young, Annu. Rev. Fluid Mech. 39 (2007) 193–215.
- [10] L. Ma, D.B. Ingham, M. Pourkashanian, E. Carcadea, J. Fuel Cell Sci. Technol. 2 (2005) 246–257.
- [11] R. Bove, S. Ubertini, J. Power Sources 159 (2006) 543–559.
- [12] V.M. Janardhanan, O. Deutschmann, J. Power Sources 162 (2006) 1192–1202.
- [13] V.M. Janardhanan, V. Heuveline, O. Deutschmann, J. Power Sources 178 (2008) 368–372.
- [14] A. Bejan, Heat Transfer, Wiley, New York, 1993.
- [15] R.K. Shah, A.L. London, Laminar Flow Forced Convection in Ducts, in: Supplement 1 to Advances in Heat Transfer, Academic Press, New York, 1978.
- [16] A. Bejan, Convection Heat Transfer, 2nd ed., Wiley, New York, 1995.
- [17] A. Bejan, Advanced Engineering Thermodynamics, 2nd ed., Wiley, New York, 1997.
- [18] J.W. Kim, A.V. Virkar, K.Z. Fung, K. Mehta, S.C. Singhal, J. Electrochem. Soc. 146 (1) (1999) 69–78.
- [19] P. Aguiar, C.S. Adjiman, N.P. Brandon, J. Power Sources 138 (2004) 120–136.
- [20] R.C. Reid, J.M. Prausnitz, B.E. Poling, The Properties of Gases and Liquids, 4th ed., McGraw Hill, New York, 1988.
- [21] C.W. Tanner, K.Z. Fung, A.V. Virkar, J. Electrochem. Soc. 144 (1) (1997) 21–30.
- [22] S.H. Chan, Z.T. Xia, J. Electrochem. Soc. 148 (4) (2001) A388–A394.
- [23] A.J. Bard, L.R. Faulkner, Electrochemical Methods—Fundamentals and Applications, 2nd ed., Wiley, New York, 2001.
- [24] D. Kincaid, W. Cheney, Numerical Analysis Mathematics of Scientific Computing, 1st ed., Wadsworth, Belmont, 1991.
- [25] H.Y. Tu, U. Stimming, J. Power Sources 127 (2004) 284–293.
- [26] J.H. Nam, D.H. Jeon, Electrochim. Acta 51 (2006) 3446–3460.